




# Efficient under visible catalysts from electrospun flexible Ag<sub>2</sub>S/TiO<sub>2</sub> composite fiber membrane

Min Dong<sup>1</sup>, Qing-Hao Li<sup>1</sup>, Ru Li<sup>2</sup>, Yu-Qian Cui<sup>1\*</sup> , Xiao-Xiong Wang<sup>2</sup>, Jian-Qiang Yu<sup>3</sup>, and Yun-Ze Long<sup>2,\*</sup>

<sup>1</sup>College of Environmental Science and Engineering, Qingdao University, Qingdao 266071, China

<sup>2</sup>Collaborative Innovation Center for Nanomaterials and Devices, College of Physics, Qingdao University, Qingdao 266071, China

<sup>3</sup>Institute of Green Chemistry and Industrial Catalysis, College of Chemistry and Chemical Engineering, Qingdao University, Qingdao 266071, China

Received: 26 August 2020

Accepted: 8 January 2021

Published online:  
22 January 2021

© The Author(s), under exclusive licence to Springer Science+Business Media, LLC part of Springer Nature 2021

## ABSTRACT

The issue of antibiotic residue and contamination has attracted significant attention. Most of the existing degradation methods are inefficient and costly. Photocatalytic technology is an up-and-coming method. Titanium dioxide (TiO<sub>2</sub>) is a photocatalyst widely used to degrade the residual antibiotics in water under ultraviolet (UV) irradiation. However, its application efficiency under visible light is poor, owing to its wide bandgap. This paper reports the successful synthesis of Ag<sub>2</sub>S/TiO<sub>2</sub> composite nanofiber membranes through electrospinning and hydrothermal processes, and adsorption and photocatalytic removal of tetracycline (TC) under visible light irradiation. Ag<sub>2</sub>S/TiO<sub>2</sub> showed excellent photocatalytic property for TC degradation compared with Ag<sub>2</sub>S and TiO<sub>2</sub>, and the efficiency was up to 70.54%. It kept high photocatalytic performance after five cycles. The detailed mechanism of TC degradation by Ag<sub>2</sub>S/TiO<sub>2</sub> was also proposed based on the radical trapping experiment and the analysis of degradation intermediates. Benefiting from the large surface area, effective photocatalysis under visible light irradiation, and excellent recyclability, Ag<sub>2</sub>S/TiO<sub>2</sub> composite fiber membranes are promising in the treatment of antibiotic wastewater.

## Introduction

Antibiotics are one of the most effective drugs to prevent and treat human bacterial infections and animal infectious diseases [1]. Among them,

tetracycline hydrochloride (TC), as an effective antibiotic, is prevalently used in the aquaculture industry and animal husbandry. After use, it cannot be absorbed or transformed completely by humans and animals [2]. Its residues and metabolites are

Handling Editor: Chris Cornelius.

Address correspondence to E-mail: bonnie\_cyq@163.com; yunze.long@163.com

noxious to aquatic and terrestrial animals and can be accumulated and spread along the food chain, leading to severe human health damage [3–5]. Therefore, the removal of antibiotic residues from the environment is significant for the ecosystem and human health.

Photocatalytic degradation of antibiotics is efficient, economical, and environmentally friendly compared with other traditional techniques, such as anaerobic digestion, biodegradation, and adsorption. Antibiotics could be converted into compounds which are readily biodegradable or organic molecules with less toxicity, thereby reducing or eliminating their antibacterial activity [6]. Titanium dioxide ( $\text{TiO}_2$ ) has better photocatalytic performance compared with other catalysts used under ultraviolet (UV) light irradiation. However, its shortcomings in the actual use process also hinder its maximum catalytic activity [7]. The wide bandgap (3.26 eV) causes it hard to collect sufficient solar energy sources; thus, light utilization efficiency is low. The electron–hole pair composite annihilation probability generated when the light source irradiated is higher, and the ratio of the generated superoxide radical to the hydroxyl group is decreased [8]. The researchers developed various schemes to modify  $\text{TiO}_2$ , such as the improvement of morphology and properties [9], metal complex [10], nonmetal complex [11], dye sensitization [12], and construction of heterogeneous structures [13]. Among them, the combination of  $\text{TiO}_2$  and other materials to construct heterostructures has been widely studied. Recently,  $\text{Ag}_2\text{S}$  has attracted significant attention due to its low toxicity and narrow bandgap [14].  $\text{Ag}_2\text{S}$  is a semiconductor material with a bandgap of about 0.84 eV which can effectively utilize visible light [15]. It can be used to modify  $\text{TiO}_2$  with a wide bandgap. For example, Ong et al. showed that the methyl orange degradation could be improved by decorating  $\text{TiO}_2$  hierarchical spheres with  $\text{Ag}_2\text{S}$  nanoparticles, and the degradation efficiency was 99.93% within 120 min [16]. Most synthesized photocatalysts still exist in powder, and they are easily reunited [17, 18]. Therefore, when these photocatalysts are used in the practical application, the drawbacks, such as cannot be recovered and recycled, still suffered.

The immobilization of  $\text{TiO}_2$  film by electrospinning technology can solve the above problems perfectly [19]. Electrostatic spinning nanofibers are widely used in wastewater treatment due to their high

porosity, small diameter, and large specific surface area. At the same time, some flexible substrate materials could be used as a support for the photocatalyst to synthesize flexible photocatalytic composite materials [20, 21]. For instance, Li et al. fabricated chitosan/g- $\text{C}_3\text{N}_4/\text{TiO}_2$  nanofibers by electrospinning to remove Cr(VI) through the photocatalytic and adsorption processes [22]. Among many polymer materials, polyvinylidene fluoride (PVDF) has excellent thermal stability, chemical corrosion resistance, mechanical strength and flexibility, thus, it is suitable to be used as a flexible photocatalytic material [23]. It can solve the problem of separating and recovering the photocatalyst from the reaction solution [24]. Recently, many researchers have used hydrothermal reaction to directly grow  $\text{TiO}_2$  on electrostatic spinning polymer fiber to obtain flexible and recyclable composite fiber membranes. Because of the simple device and using cheaper, it has been widely used in nanocrystal preparation [25, 26]. Using the hydrothermal approach to combine  $\text{TiO}_2$  and  $\text{Ag}_2\text{S}$  onto flexible PVDF fiber membrane can solve the problem that photocatalysis is difficult to recover and generate  $\text{Ag}_2\text{S}/\text{TiO}_2$  heterojunction, which could widen the available light area to visible light area and prevent photoinduced electron–hole pairs in recomposing effectively. Hence, the photocatalytic performance of the catalyst can be improved by the above characteristics.

In this study, a flexible and recyclable  $\text{Ag}_2\text{S}/\text{TiO}_2$  composite fiber membrane with visible light response was successfully prepared by uniting the electrostatic spinning method and the hydrothermal reaction. Under visible light, the TC degradation performance of the prepared membranes with different amounts of composite  $\text{Ag}_2\text{S}$  was investigated. A composite membrane with better performance was selected for reference for subsequent research. Besides, according to the radical trapping experiment, and analyses of total organic carbon (TOC) and degradation intermediates, a possible mechanism was proposed to explain the TC degradation.

## Experimental

### Chemicals

Polyvinylidene fluoride (PVDF,  $M_w \approx 550000$ ) was obtained from Sigma-Aldrich (St. Louis, MO.). N,

N-dimethylformamide (DMF), tetrabutyl titanate (TBOT), acetone, thiourea ( $\text{CH}_4\text{N}_2\text{S}$ ), silver nitrate ( $\text{AgNO}_3$ ), ammonium oxalate (AO), L-ascorbic acid (L-AA) and isopropanol (IPA) were purchased from Sinopharm Chemical Reagent Co, Ltd. TC and furfuryl alcohol (FFA) were provided by Shanghai Macklin Biochemical Co., Ltd. These chemical reagents used as received under analytical grade, deionized and high-purity water were used during all the experiments.

### Synthesis of TBOT-PVDF fibers

Mix 4.0 g of PVDF with 10.0 g DMF and 10.0 g acetone in a conical flask, and then the mixture was magnetically stirred under water-bath heating at 40 °C until it became transparent. Afterward, 10.0 mL TBOT was added to the above solution and under ultrasonic treatment for 1 h at 40 °C to prepare TBOT-PVDF mixed solution. Then, 5.0 mL of the precursor solution was filled into a syringe, and TBOT-PVDF fiber membranes are obtained by electrospinning. The parameters for preparing the fiber membrane in the electrospinning process are as follows: The propulsion speed is set to 2.0 mL  $\text{h}^{-1}$ . Then, the aluminum foil was wrapped on a stainless steel drum as a fiber collector. The drum's rotation speed was 240 rpm, the direct current voltage source was set at 11 kV, and the spacing between the syringe and the drum was 15 cm. The electrospun TBOT-PVDF fiber was dried at 60 °C for 10 h to fully evaporate the residual solvent. Eventually, fiber's clip the size into 2.5 cm  $\times$  2.5 cm to facilitate following synthesis operations.

### Fabrication of $\text{Ag}_2\text{S}/\text{TiO}_2$ fibers

$\text{AgNO}_3$  and  $\text{CH}_4\text{N}_2\text{S}$  were mixed in 30 mL high-purity water in the molar ratio of 1:1. The mixture was stirred for 30 min and then transferred to a 50 mL Teflon reaction kettle. After that, the pieces of TBOT-PVDF were soaked into it. The reactor was put in an electrothermal blast oven kept at 150 °C for 24 h. Lastly, the products were rinsed with ethanol and high-purity water and then dried under 50 °C for 10 h to obtain a flexible  $\text{Ag}_2\text{S}/\text{TiO}_2$  composite nanofiber membrane. For comparison, the additive contents of  $\text{AgNO}_3$  and  $\text{CH}_4\text{N}_2\text{S}$  were 0.1, 0.2, and

0.5 mmol, respectively. Also, the composite materials were labeled as Ag0.1, Ag0.2, and Ag0.5, respectively. Following the above steps, replacing the TBOT-PVDF membrane with a pure PVDF membrane, and when the addition amounts of  $\text{AgNO}_3$  and  $\text{CH}_4\text{N}_2\text{S}$  were both 0.5 mmol, an  $\text{Ag}_2\text{S}$  fiber membrane could be obtained.

### Characterization

The shape and structure of composited materials were characterized by scanning electron microscopy (SEM), energy-dispersive spectrum (EDS) as well as transmission electron microscopy (TEM) analyses. The Rigaku SmartLab X-ray diffractometer was used to measure the X-ray diffraction spectrum (XRD) pattern in the  $2\theta$  range of 20° to 80°. The photoluminescence (PL) spectrum of the sample at the excitation wavelength of 320 nm was measured by the Hitachi F-4600 fluorescence spectrometer to study the recombination efficiency of photoinduced charge. The Brunauer–Emmett–Teller (BET) measures the surface area as well as pore size distributions. The UV–Visible absorption spectroscopy was taken on an UV-3900 spectrophotometer. The TOC assays were conducted on Shimadzu TOC-L analyzer. The degradation intermediates of TC were identified by an Ultimate 3000 UHPLC-Q Exactive liquid chromatography–mass spectrometer (LC–MS) (Thermo Scientific, US).

### Adsorption measurements

The prepared membrane catalysts were added into tubes containing 50 mL of 20 mg  $\text{L}^{-1}$  TC solution. The adsorption experiments were carried out in a photocatalytic reactor in the dark at room temperature (25 °C). The absorbance of TC at 357 nm was measured by spectrophotometer to survey the consistency of residual TC in the solution. The following formula calculated the adsorption competence  $q_e$  of the composite membrane in adsorbing TC:

$$q_e = \frac{(C_0 - C_e)}{m} V \quad (1)$$

where  $C_0$  (mg  $\text{L}^{-1}$ ) is the starting and  $C_e$  (mg  $\text{L}^{-1}$ ) is the equilibrium concentration of TC,  $V$  (L) is the TC volume, and  $m$  (g) is the weight of the adsorbent used.

## Photocatalytic degradation experiment

The photocatalytic performance of the membranes was evaluated by decomposing the simulated pollutant TC ( $20 \text{ mg L}^{-1}$ ) at room temperature on a photocatalytic reactor, composed of an 800 W Xe lamp with 420 nm cutoff filters as a visible light irradiation source. In this experiment, the prepared different photocatalysts were, respectively, placed in test tubes containing 50 mL TC and magnetically stirred for 30 min under dark conditions to achieve the adsorption–desorption equilibrium. At regular intervals, the appropriate amount of solution was collected to measure the absorbance at 357 nm. After the analysis, these aliquots were quickly returned to test tubes to ensure approximately equal solution volumes after each measurement. The TC's photodegradation efficiency is expressed as  $C/C_0$ , where  $C_0$  and  $C$  are the absorbances at initial and time  $t$  of TC, respectively. Figure 1 shows the schematic diagram of the synthesis of  $\text{Ag}_2\text{S}/\text{TiO}_2$  nanofibers and the application of nanofibers in the photocatalytic process.

## Trapping experiment

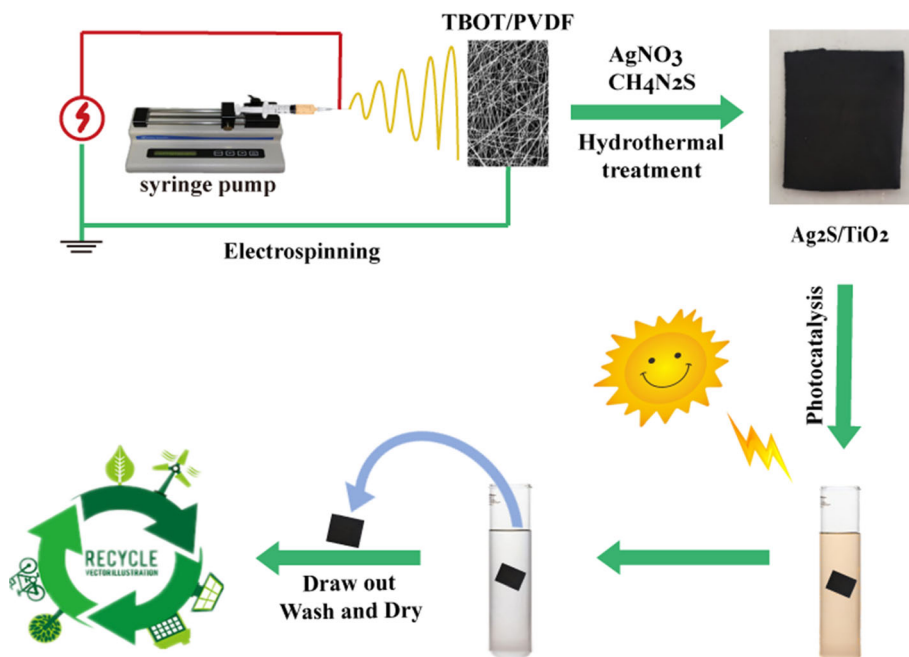
In order to identify the reactive radicals, which are the main factors in the degradation of TC in the

system, we carried out the free radicals trapping experiments. There are 1 mmol of AO, FFA, IPA, and L-AA were used as scavengers for the photoinduced hole ( $\text{h}^+$ ), singlet oxygen ( $^1\text{O}_2$ ), hydroxyl radical ( $\cdot\text{OH}$ ), and superoxide radical ( $\cdot\text{O}_2^-$ ), respectively [27, 28]. After the dark reaction, the scavengers were put into TC solutions, and then the experiments were carried out one by one according to the above procedure.

## Degradation intermediates identification

The degradation intermediates of TC were identified by a LC–MS equipped with an Eclipse Plus C18 column ( $100 \text{ mm} \times 4.6 \text{ mm}$ ,  $5 \mu\text{m}$ ). Elution was carried out by 0.1% (v/v) formic acid aqueous solution (A) and acetonitrile (B) at a flow rate of  $0.3 \text{ mL min}^{-1}$ . The injection volume was  $10 \mu\text{L}$ , and the column temperature was  $30 \text{ }^\circ\text{C}$ . The gradient elution conditions were 80% A + 20% B. MS was carried out in positive ion mode using an electrospray ionization source (ESI) under the following conditions: spray voltage, 3.8 kV; gas rate,  $40 \text{ mL}^{-1}$ ; capillary temperature,  $320 \text{ }^\circ\text{C}$ ; gas temperature,  $300 \text{ }^\circ\text{C}$ . The mass range of MS scanning is 100–600 m/z.

**Figure 1** Schematic diagram of the synthesis of  $\text{Ag}_2\text{S}/\text{TiO}_2$  nanofibers and its application for the removal of TC.





## Results and discussion

### Characterization of synthetic materials

#### Morphology analysis

The morphology analysis of the samples was further determined by SEM and HRTEM. As shown in Fig. 2a, b, c, d, e, f, it can be found that the nanofibers have different orientations, and fiber films are formed in a cross-overlapping manner. Figure 2a, b shows that TBOT nanofibers synthesized by electrospinning remain fibrous after being converted into  $\text{TiO}_2$  by the

hydrothermal method. Moreover,  $\text{TiO}_2$  particles were uniformly distributed on PVDF fibers with a diameter of about 20 nm. The evenly distributed  $\text{Ag}_2\text{S}$  nanoparticles in irregular shapes were compactly attached to PVDF fibers (Fig. 2c, d), and the diameter is mostly 400 to 600 nm (Fig. S1). Figure 2e, f shows the  $\text{Ag}_0.1$ . From the figure, it can be observed that  $\text{TiO}_2$  and  $\text{Ag}_2\text{S}$  are evenly distributed on PVDF fibers. However, the diameter of  $\text{Ag}_2\text{S}$  is mostly 200 nm (Fig. S1), which is smaller than that of  $\text{Ag}_2\text{S}$  particles, as shown in Fig. 2d. This indicates that the size of  $\text{Ag}_2\text{S}$  particles increases with increasing molar ratio. This may be due to the higher concentration of

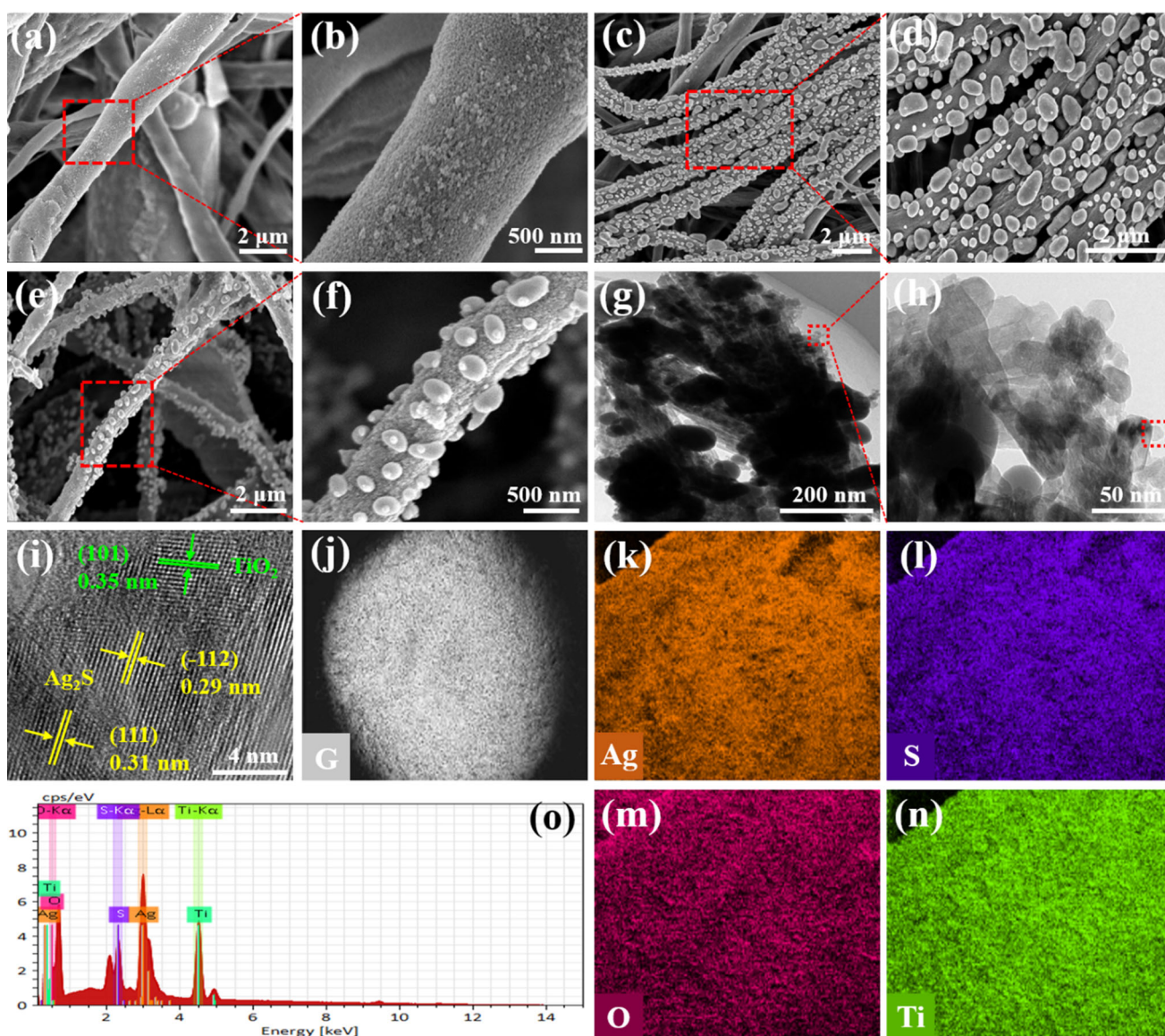


**Figure 2** Morphological characteristics of nanofibers. SEM images: **a, b**  $\text{TiO}_2$ ; **c, d**  $\text{Ag}_2\text{S}$  (0.5 mmol); **e, f**  $\text{Ag}_0.1$ ; **g, i** TEM and HRTEM images of  $\text{Ag}_0.1$ ; **j, o** SEM-EDS elemental mapping and EDS pattern of  $\text{Ag}_0.1$ .

$\text{CH}_4\text{N}_2\text{S}$  in solution, which leads to chelation between  $\text{CH}_4\text{N}_2\text{S}$  molecule and  $\text{Ag}^+$ ; thus, reducing the reaction rate of  $\text{Ag}^+$  and  $\text{S}^{2-}$ , making the  $\text{Ag}_2\text{S}$  crystal grow rapidly [29]. Figure 2g, h is the TEM images of Ag0.1, which shows that small particles of  $\text{TiO}_2$  and large particles of  $\text{Ag}_2\text{S}$  are loaded on PVDF fibers. Figure 2i, the lattice fringes analysis of HRTEM, shows that  $d = 0.35$  nm, 0.29 nm, and 0.31 nm correspond to (101) crystallographic planes of  $\text{TiO}_2$ , (-112) and (111) of  $\text{Ag}_2\text{S}$ , respectively [30, 31]. The above analysis demonstrated that the  $\text{Ag}_2\text{S}$  and  $\text{TiO}_2$  have been deposited on the surface of PVDF fibers, and  $\text{Ag}_2\text{S}/\text{TiO}_2$  composite fibers membrane have been successfully synthesized.

To further confirm the element composition and distribution of Ag0.1, SEM-EDS mapping was conducted. As shown in Fig. 2j, k, l, m, n, the SEM image and the corresponding mapping pictures show the highly distributive Ag, S, O, and Ti elements in the Ag0.1 nanofiber. The EDS analysis revealed the existence of the above elements, as shown in Fig. 2o.

### XRD analyses

XRD analyses studied the crystallinity and purity of nanofibers synthesized at different concentrations. Figure 3 shows the patterns of the prepared  $\text{TiO}_2$  and  $\text{Ag}_2\text{S}$  composites. Figure 3a shows that the diffraction signals at  $25.4^\circ$ ,  $37.9^\circ$ ,  $48.3^\circ$ ,  $54.1^\circ$ ,  $62.9^\circ$ , and  $75.1^\circ$  were pointed to the (101), (004), (200), (105), (204),

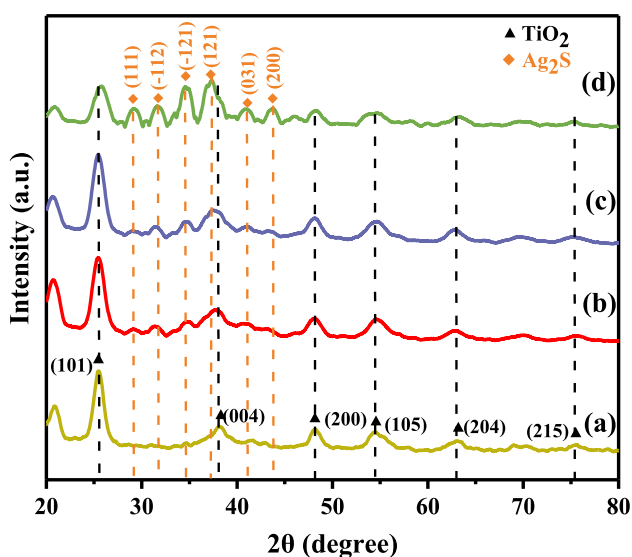


**Figure 3** XRD patterns of materials: a  $\text{TiO}_2$  nanofibers; b Ag0.1 nanofibers; c Ag0.2 nanofibers; d Ag0.5 nanofibers.

and (215) crystal planes of  $\text{TiO}_2$ , respectively [32]. In Fig. 3b, c, the peaks at  $29.0^\circ$ ,  $31.4^\circ$ ,  $34.4^\circ$ ,  $36.8^\circ$ ,  $40.7^\circ$ , and  $43.3^\circ$  corresponded to the (111), (-112), (-121), (121), (031), and (200) of  $\text{Ag}_2\text{S}$  [33]. The magnitude of the peaks of  $\text{Ag}_2\text{S}$  increased significantly with the rise of the content of  $\text{Ag}_2\text{S}$ . It can also be observed that as the proportion of  $\text{Ag}_2\text{S}$  added increases, the characteristic peak intensity of  $\text{TiO}_2$  becomes lower while  $\text{Ag}_2\text{S}$  becomes higher. Therefore, it can be inferred from the results of XRD that  $\text{Ag}_2\text{S}/\text{TiO}_2$  composite membranes have been synthesized with success by the techniques of electrostatic spinning and hydrothermal synthesis.

### PL spectra

In general, PL spectroscopy can be used for the analysis of photoproduced electron-hole pair complex annihilation and separation. The charge transfer of electrons and holes of semiconductors can be studied by the information displayed in the spectrum, and the photocatalyst activity is severely affected by the recombination of photogenic electron-hole pair [34]. Figure 4 shows the PL spectra of  $\text{TiO}_2$  and  $\text{Ag}_2\text{S}$  nanofiber films doped with different proportions of  $\text{Ag}_2\text{S}$ . The PL spectra have the excitation wavelengths of 320 nm. It can be observed that all the synthesized  $\text{Ag}_2\text{S}$  nanofiber membranes have emission peaks near the edge of the band around 423 nm without migration. Besides, all samples have four emission peaks between 440 nm (2.82 eV) and 495 nm (2.51 eV), caused by oxygen vacancy defects generated during the preparation process [35].

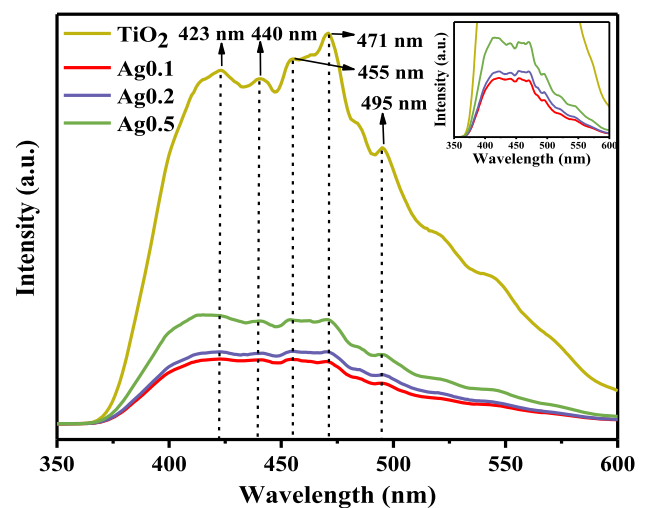


**Figure 4** PL spectra of materials.

The inferior intensity of the PL spectral curve, the lower recombination efficiency of the photogenerated electron–hole pairs, it means that the photocatalytic activity is higher [36]. Therefore, a proper proportion of  $\text{Ag}_2\text{S}$  composite is propitious to increase the photocatalytic degradation efficiency of pollutants. Among all  $\text{Ag}_2\text{S}$  nanofibers, Ag0.1 has the lowest emission peak intensity, indicating the longest lifetime of the electron–hole separation. Combining SEM and XRD analysis, with the  $\text{Ag}_2\text{S}$  doping content increasing, the average grain size becomes bigger, which may be accompanied by the existence of lattice defects and can accelerate the recombination between electron and hole.

### UV–visible absorption

The optical properties of  $\text{TiO}_2$ , Ag0.1, Ag0.2, and Ag0.5 were studied by UV–visible diffused reflectance spectroscopy. According to Kubelka–Munk function, the reflectivity is converted into absorption value [37]:

$$F(R) = \frac{(1 - R)^2}{2R} \quad (2)$$

Here,  $R$  is the reflection (%), and  $F(R)$  is the Kubelka–Munk function. As shown in Fig. 5a,  $\text{TiO}_2$  shows an absorption edge near 380 nm, corresponding to its bandgap of 3.26 eV. After the combination of  $\text{Ag}_2\text{S}$ , the absorption value of composite fiber membranes under the visible light range is much higher than that of  $\text{TiO}_2$ . It increases the light absorption capacity of  $\text{TiO}_2$  under visible light,

resulting in more electron–hole pairs, which can create higher photocatalytic activity.

Formula (2) applied to the reflection phenomenon of the semiconductor surface is [38]:

$$(Ah\nu)^n = B(h\nu - E_g) \quad (3)$$

Here,  $h$  is the Planck constant,  $\nu$  is the frequency of light,  $B$  is a physical quantity related to the material,  $E_g$  is the bandgap energy value,  $A$  is the absorbance,  $n$  is 1/2 for indirect bandgap semiconductors, and direct bandgap type semiconductor is 2. The energy intercept of a plot of  $(Ah\nu)^2$  against  $(h\nu)$  yields  $E_g$ , as shown in Fig. 5b. The  $E_g$  of  $\text{TiO}_2$ , Ag0.1, Ag0.2, and Ag0.5 was calculated as 3.26, 2.19, 2.64, and 2.85 eV, respectively. It is proposed that an appropriate amount of Ag source can deposit  $\text{Ag}_2\text{S}$  on the PVDF fiber uniformly, which gives rise to the contact surface between  $\text{TiO}_2$  and  $\text{Ag}_2\text{S}$  larger, leading to the absorption boundary of the catalysts moved toward the longwave region, i.e., a redshift phenomenon occurred [39]. However, when the deposited amount of  $\text{Ag}_2\text{S}$  is too high, the overlapping between  $\text{Ag}_2\text{S}$  particles will hinder the transport of photogenerated electrons, thereby reducing the exposure rate of the active center [40].

### BET analysis

The bore diameter and specific surface area distribution of  $\text{TiO}_2$  and  $\text{Ag}_2\text{S}/\text{TiO}_2$  fiber membranes were analyzed. Figure 6a shows that the curves of the  $\text{TiO}_2$  membrane and the  $\text{Ag}_2\text{S}/\text{TiO}_2$  fiber membrane were

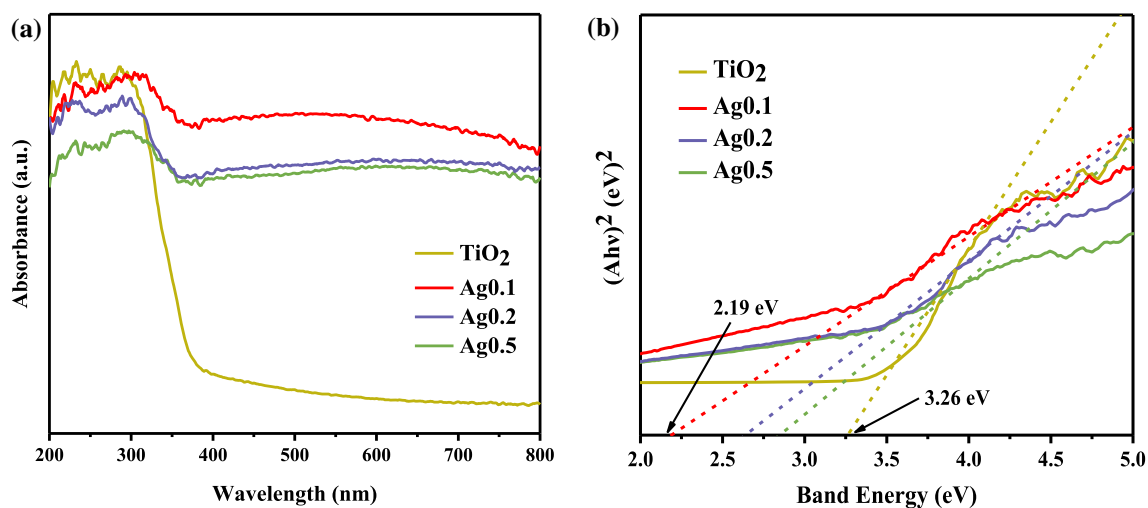


**Figure 5** a UV–Vis absorption of materials; b Bandgap of  $\text{Ag}_2\text{S}/\text{TiO}_2$ .



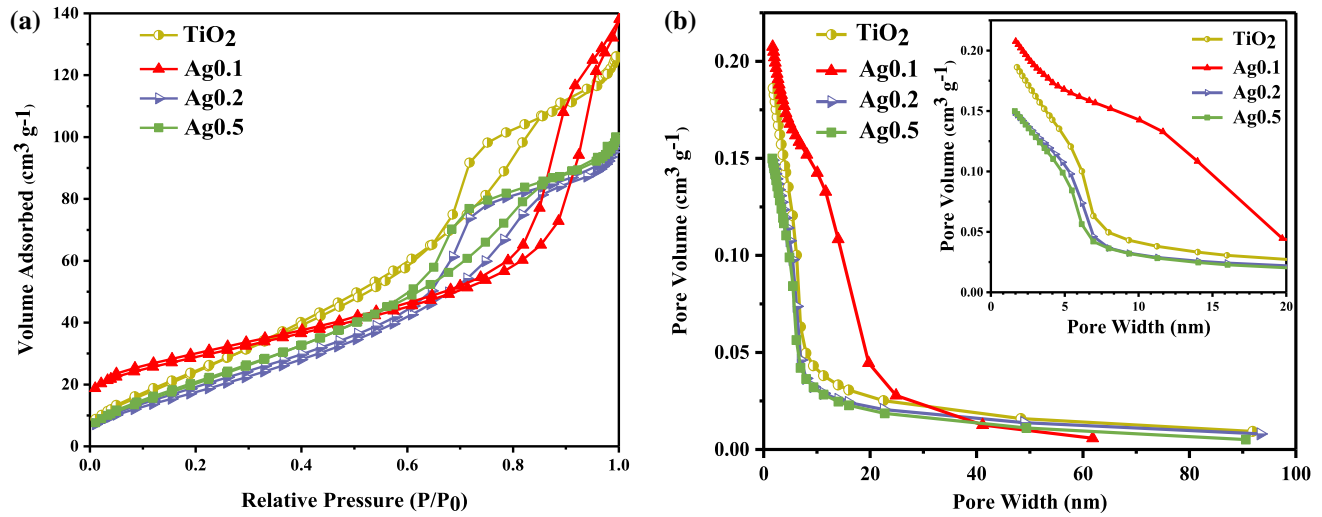


**Figure 6** a Nitrogen adsorption–desorption isotherm; b Pore size distribution curves of TiO<sub>2</sub> and Ag<sub>2</sub>S/TiO<sub>2</sub> composite nanofibers.

identified as type IV isotherms in the range of 0.55–1.0, and the appearance of manifest H3-type hysteresis loops indicates the existence of mesoporous structures [37]. All the properties of mesoporous samples were calculated. The pore diameters of all the samples are distributed in the range of 2–14 nm, as shown in Fig. 6b. Table S1 shows that the pore size of the Ag0.1 fiber membrane is larger than that of the TiO<sub>2</sub> membrane, and the average pore diameter increases from 5.4 to 7.9 nm. With the rise of the content of Ag<sub>2</sub>S, the pore size of the fiber membrane decreases gradually. It can be seen that the doping amount of Ag<sub>2</sub>S plays a significant role in increasing the specific surface area of the nanocomposite membranes.

### Adsorption experiments

Figure 7a shows the effect of adsorption time on TC. It is evident that as the reaction progresses, the adsorption amount gradually increases, and all materials reach equilibrium within 60 min. In the first 5 min, all the materials showed a rapid reaction rate, and the highest adsorption capacity was almost 80% of the equilibrium. This phenomenon can be attributed to the sufficient active sites on the adsorbent at the beginning of the reaction. The adsorption sites gradually become saturated after being occupied by TC molecules during the reaction process. Therefore, the adsorption amount slowly increases in the later stage and finally remains unchanged. The whole reaction process can almost reach equilibrium within

the first 30 min. Among them, the adsorption capacity of Ag0.1 is 2.14181 mg g<sup>-1</sup>, which is better than any other samples.

The experimental data are fitted with pseudo-first-order and pseudo-second-order kinetic models. These models are expressed as follows [41, 42]:

$$\ln(q_m - q) = \ln q_m - k_1 t \tag{4}$$

$$\frac{t}{q} = \frac{1}{k_2 q_m^2} + \frac{t}{q_m} \tag{5}$$

where  $k_1$  (min<sup>-1</sup>) and  $k_2$  (g mg<sup>-1</sup> min<sup>-1</sup>) are the rate constants for pseudo-first-order and pseudo-second-order kinetic models, respectively;  $q_m$  and  $q$  (mg g<sup>-1</sup>) are the adsorption quantity of equilibrium time and any time  $t$  (min), respectively.

The kinetic fitting results and related parameters are shown in Fig. 7b, c and Table S2. These results showed that the correlation coefficients ( $R^2$ ) of the pseudo-second-order are all significantly bigger than 0.999, which exceeds the pseudo-first-order kinetic model, revealing that the pseudo-second-order kinetic model is more in line with the reaction process. Therefore, the adsorption procedure of TC on the composite fiber membrane is mainly chemical adsorption.

### Photocatalysis experiments

The photocatalytic performance of Ag<sub>2</sub>S/TiO<sub>2</sub> fiber membranes synthesized by different concentrations of Ag<sub>2</sub>S was confirmed by monitoring the concentration change of TC solution with continuous-time



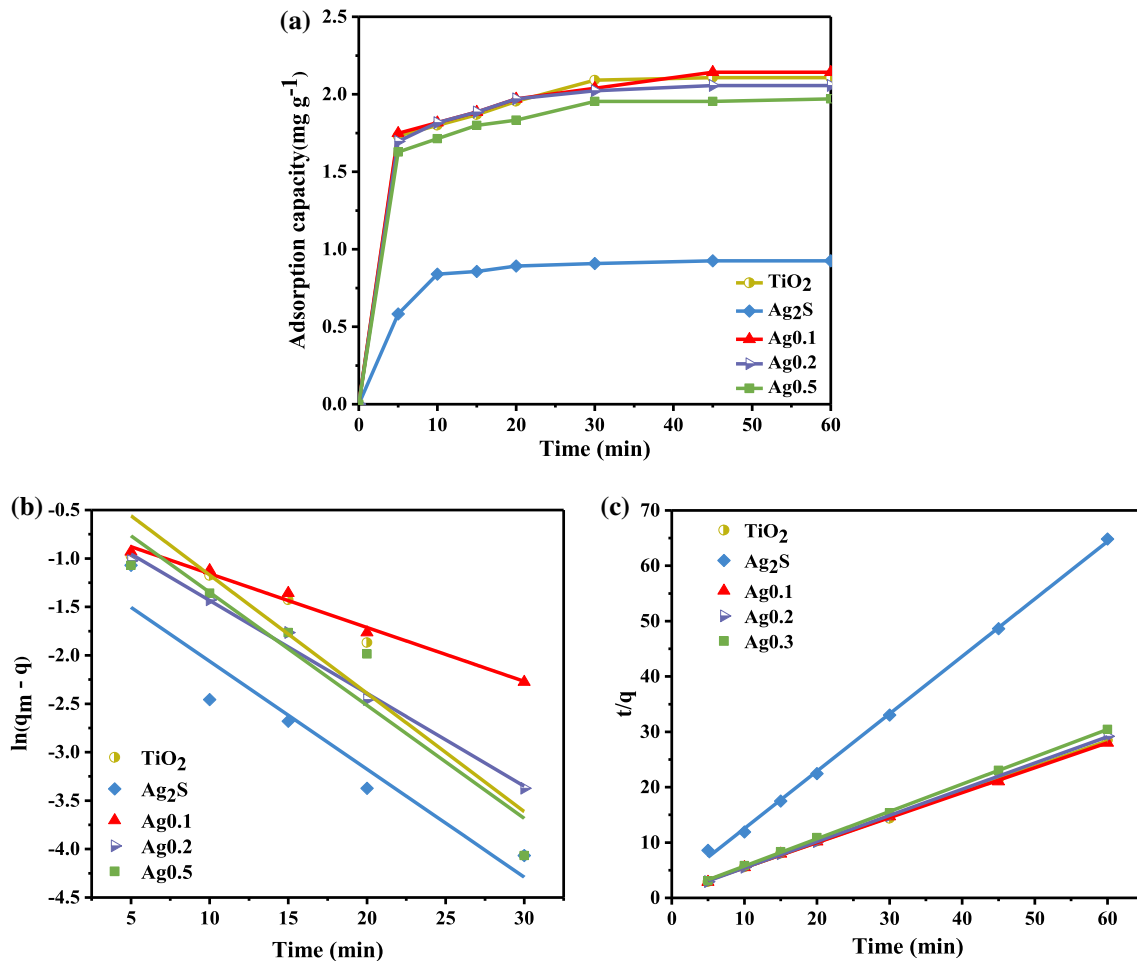


**Figure 7** **a** Effect of contact time on the TC absorption; **b** Pseudo-first-order model; **c** Pseudo-second-order model.

under visible light. For comparison, the photocatalytic performance of TiO<sub>2</sub> and Ag<sub>2</sub>S films was measured under the same conditions. As shown in Fig. 8a, before formally starting the light, dark state adsorption was performed for 30 min to ensure that an adsorption–desorption equilibrium state was attained. The concentration change of TC solution without catalyst and Ag<sub>2</sub>S fiber membrane during the whole photocatalysis process can be ignored, indicating that TC is stable under visible irradiation, and Ag<sub>2</sub>S fiber membrane has almost no photodegradation effect on TC. Ag<sub>2</sub>S/TiO<sub>2</sub> nanofiber membrane has higher photocatalytic efficiency for TC under 240 min irradiation compared with the 44.32% photocatalytic efficiency of TiO<sub>2</sub> nanofiber membrane. The photocatalytic efficiencies of Ag0.1, Ag0.2, and Ag0.5 were 70.54%, 60.89%, and 58.10%, respectively. Moreover, Ag0.1 has the highest photodegradation efficiency, which is about 1.59 times higher than TiO<sub>2</sub>.

The degradation process of TC can be fitted by a first-order kinetic formula [43]:

$$-\ln\left(\frac{C}{C_0}\right) = kt \quad (6)$$

Here,  $C$  (mg L<sup>-1</sup>) is the concentration of TC at the light time  $t$ ,  $C_0$  (mg L<sup>-1</sup>) is the initial concentration,  $t$  (min) is the time of visible light irradiation,  $k$  (min<sup>-1</sup>) is the degradation rate constant that can be calculated using the formula. The larger value of  $k$  will lead to a higher degradation rate and reactivity [44]. By calculation, the values of  $k$  in Fig. 8b corresponding to TiO<sub>2</sub>, Ag<sub>2</sub>S, Ag0.1, Ag0.2, and Ag0.5 are  $3.60 \times 10^{-5} \text{ min}^{-1}$ ,  $3.46 \times 10^{-5} \text{ min}^{-1}$ ,  $3.61 \times 10^{-3} \text{ min}^{-1}$ ,  $4.08 \times 10^{-3} \text{ min}^{-1}$ , and  $1.01 \times 10^{-3} \text{ min}^{-1}$ , respectively. Among them, Ag0.1 has the fastest catalytic degradation rate, which also follows the analysis of the PL and UV–Visible absorption. These results demonstrate that the Ag<sub>2</sub>S/

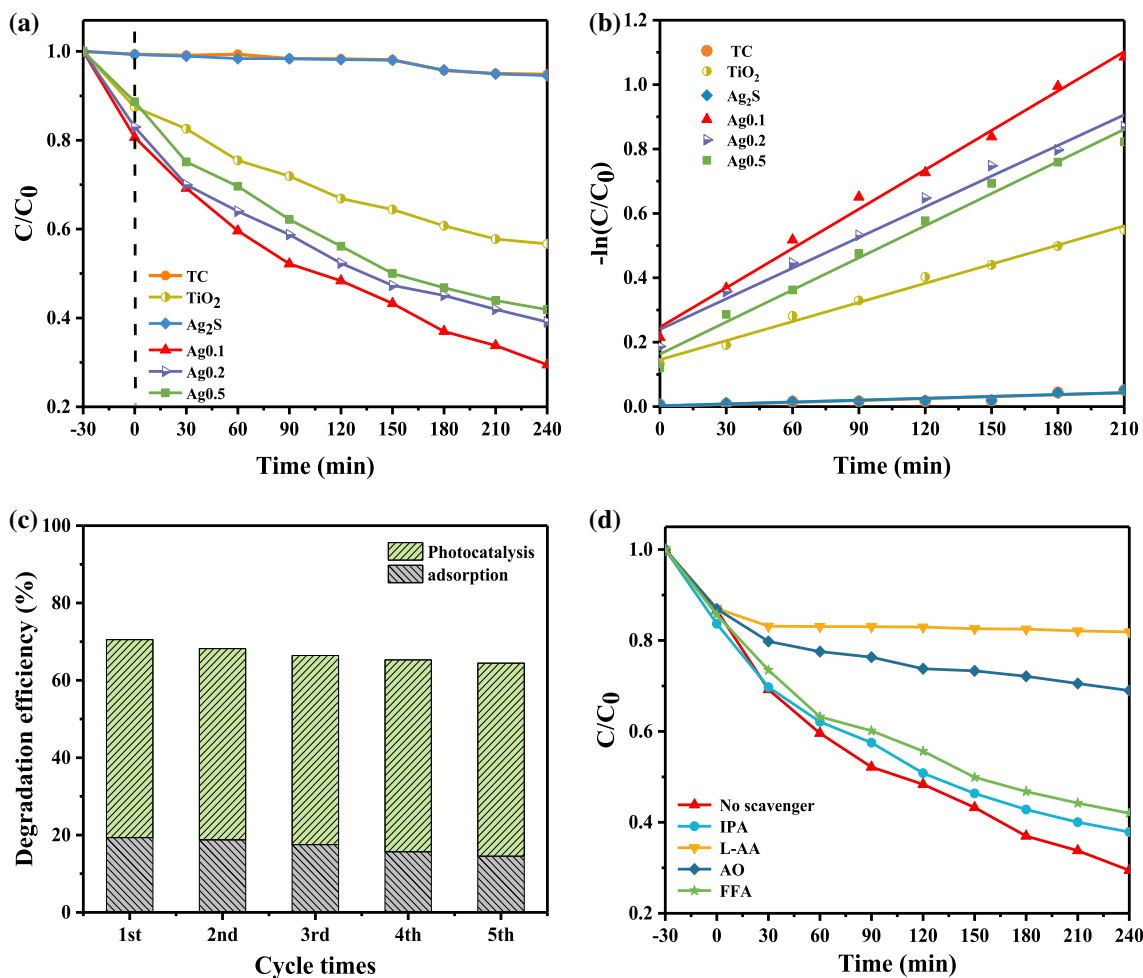


**Figure 8** a Photocatalytic degradation of TC with different photocatalyst samples under visible light illumination; b Plots of  $-\ln(C/C_0)$  versus  $t$  of different photocatalysts; c Photocatalytic

degradation of TC by Ag0.1 sample in repeated experiments; d Trapping experiments for TC.

TiO<sub>2</sub> composite nanofiber membrane can effectively degrade TC under the proper proportion.

The stability of photocatalyst plays a significant role in practical applications. Five-cycle experiments of Ag0.1 were conducted under the same conditions to evaluate the reusability of Ag<sub>2</sub>S/TiO<sub>2</sub> composite nanofiber membranes. Figure 8c shows that the removal efficiency of TC by Ag0.1 reached 64.42% after five cycles, which was 6.42% lower than that of the first time. The above evidence indicates that the Ag<sub>2</sub>S/TiO<sub>2</sub> composite nanofiber membrane has excellent stability in the catalytic process.

In this study, the prepared photocatalyst was compared with other reported TiO<sub>2</sub> photocatalysts modified by different methods for the degradation of TC under the irradiation of different types of light sources. The results are shown in Table S3. Under

different light sources, on the issue of the removal efficiency of TC, the Ag<sub>2</sub>S/TiO<sub>2</sub> catalyst obtained in this study is close to or even better than other X-TiO<sub>2</sub> catalysts prepared by previous researches. Based on catalyst stability and recyclability, this study has been conducted five times, and it maintains the best stability. In general, the recyclable photocatalyst prepared in this study has a higher removal efficiency of TC under visible light. This shows a high utility of our photocatalyst in actual wastewater treatment [45–50].

Figure 8d shows the results of the trapping experiment results. The degradation efficiency of TC after the addition of IPA and FFA is reduced, but it is inconspicuous, suggesting that the ·OH and <sup>1</sup>O<sub>2</sub> rarely participate in the degradation process of TC. However, the degradation efficiency of TC decreased

significantly after adding AO and L-AA, which implied that  $h^+$  and  $\cdot O_2^-$  played a central role in degrading TC.

### Analysis of TOC and the possible intermediates of TC photodegradation

It is of great significance to carry out TOC analysis to confirm main components after TC degradation. Figure 9a is the TOC concentration of TC solution at different time and Fig. 9b compares the degradation rate of TC and the mineralization efficiency of TOC. When the photocatalytic reaction lasted for 240 min, the degradation rate of TC was 70.54%, while the mineralization rate of TOC was 33.06%. After 360 min, the mineralization rate of TOC reached 42.07%. This indicates that TC is degraded into small molecule organic matter at first, and finally into inorganic matter,  $CO_2$ , and water. To better understand the process of photocatalytic degradation of TC, the intermediate products during the TC photodegradation were investigated and performed by LC-MS. Figure S2 shows the MS spectra and speculated molecular formula of all products (after 120 min of degradation). According to the detected intermediates, the related reports, and references, two possible degradation pathways of TC were proposed and interpreted, as shown in Fig. 10. Pathway I explains the hydroxylation process. TC was first converted into TC1 and TC2 by hydroxylation, as studied by Deng [51]. The carbon–oxygen double bond on TC2 was attacked by  $\cdot OH$ , resulting in TC3 compound formation. Pathway II is the process of TC being

degraded gradually. After being attacked by the main reactive species, TC underwent dehydroxylation, deamination, deacetylation, and opening of benzene rings. The TC molecules were first attacked by  $\cdot O_2^-$ , leading to the formation of TC4 from the detachment of hydroxyl groups. It then underwent a deamination reaction to form TC5, which is consistent with the previous results of Deng et al. [52]. Afterward, the loss of N dimethyl group generated the product TC6. The generation of TC7 was attributed to the dealdehyde reaction of TC6. Passing through a ring-opening reaction, it degraded to TC8. Then, the TC8 was fragmented into TC9, TC10, TC11, and TC12 through dehydroxylation, the opening of benzene rings, and an addition reaction. Finally, these intermediates were mineralized to  $CO_2$ ,  $H_2O$ , and other inorganic ions at the end [53].

### Mechanism of the removal of TC

The band edge positions of  $TiO_2$  and  $Ag_2S$  were estimated to explore the possible photocatalytic mechanism. The conduction band (CB) and valence band (VB) potentials were calculated using the following formulas [38, 54]:

$$E_{VB} = X - E_e + 0.5E_g \quad (7)$$

$$E_{CB} = E_{VB} - E_g \quad (8)$$

Here,  $E_{VB}$  is the VB edge potential,  $E_{CB}$  represents the CB edge potential,  $X$  is the absolute electronegativity of the semiconductor,  $E_e$  is the energy of free electrons on the hydrogen scale (about 4.5 eV), and  $E_g$  signifies the bandgap of the semiconductor. Using

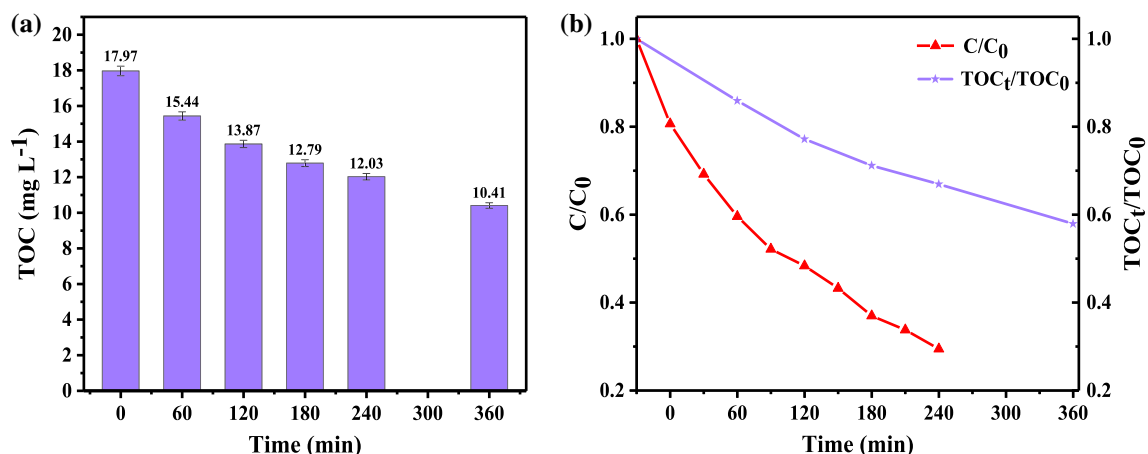


**Figure 9** **a** The TOC concentration of TC solution at different time; **b** Comparison between the degradation rate of TC and the mineralization efficiency of TOC.

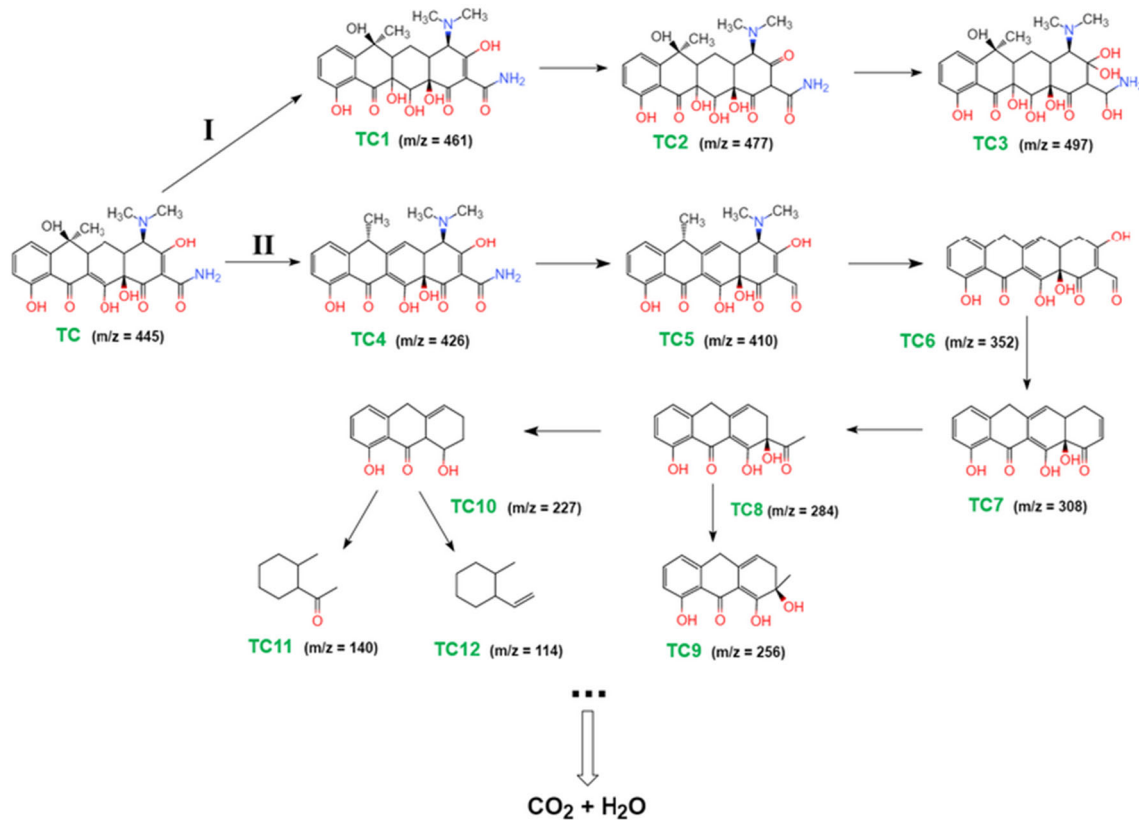


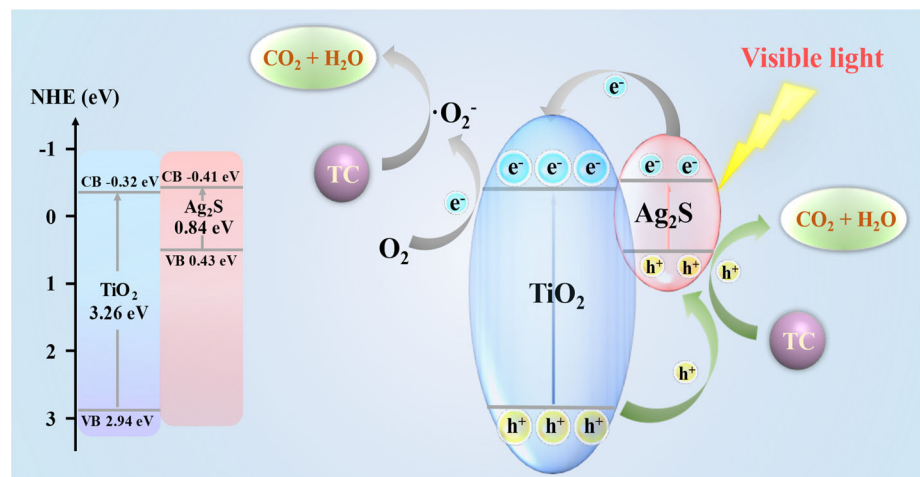
**Figure 10** Intermediates analysis and possible degradation pathways of TC degradation by  $\text{Ag}_2\text{S}/\text{TiO}_2$ .

the above formulas, the  $E_{CB}$  and  $E_{VB}$  of  $\text{Ag}_2\text{S}$  are  $-0.41$  eV and  $0.43$  eV, respectively, which is very desirable for photosensitization of  $\text{TiO}_2$  with corresponding  $E_{CB}$  and  $E_{VB}$  of  $-0.32$  eV and  $2.94$  eV, respectively.

From the results of the above tests and characterizations, we deduce the possible photocatalytic degradation mechanism of  $\text{Ag}_2\text{S}/\text{TiO}_2$  for TC, as

shown in Fig. 11. For these composite nanofiber membranes, the large specific surface area of nanofibers prepared by electrospinning provides more adsorption and photoreaction sites, which are essential for photocatalytic degradation of TC [55]. Under visible light irradiation, the  $e^-$  of  $\text{Ag}_2\text{S}$  and  $\text{TiO}_2$  excitedly transfer from their VB to CB, leading to an equal number of  $h^+$  left in VB. The  $e^-$  on the CB

**Figure 11** The photocatalytic mechanism for the TC removal.





of  $\text{Ag}_2\text{S}$  is quickly moved to the CB of  $\text{TiO}_2$  through the contact interface since the  $E_{\text{CB}}$  of  $\text{Ag}_2\text{S}$  is lower than that of  $\text{TiO}_2$ . Accordingly,  $\text{h}^+$  will be moved from the VB of  $\text{TiO}_2$  to the  $\text{Ag}_2\text{S}$  [16]. The  $\text{e}^-$  transmitted to the CB of  $\text{TiO}_2$  reacted with the  $\text{O}_2$  dissolved solution to form  $\cdot\text{O}_2^-$ , while the  $\text{h}^+$  migrated to the VB of  $\text{Ag}_2\text{S}$  and was involved in the degradation of TC [56]. In this photocatalytic reaction system, TC is degraded as an electron acceptor, and  $\cdot\text{O}_2^-$  and  $\text{h}^+$  are the primary active substances. Thus, it is clear that the catalyst gap width is reduced after the formation of the heterojunction of  $\text{Ag}_2\text{S}/\text{TiO}_2$ . The available light region can be widened from the ultraviolet area to the visible light by the narrow bandgap of  $\text{Ag}_2\text{S}$ . The heterojunction can also prevent the recombine of photoproduced electron-hole pairs effectively and prolong the lifetime of charge carriers under visible irradiation. These indicate that the performance of photocatalyst is improved.

## Conclusion

In summary,  $\text{TiO}_2$  and  $\text{Ag}_2\text{S}$  were loaded on PVDF nanofibers successfully under the combination of electrostatic spinning and hydrothermal synthesis. The degradation efficiency of TC by Ag0.1 composite fiber membrane under visible light was up to 70.54%, which is about 1.59 times higher than  $\text{TiO}_2$ . The photocatalytic activity's enhancement is ascribed to the formation of  $\text{Ag}_2\text{S}/\text{TiO}_2$  heterostructures, which can significantly promote the transfer of photoinduced carriers and improve the photocatalytic efficiency. The trapping experiment and degradation intermediates analysis were contributed to understanding the reaction mechanism, and it proves that  $\text{h}^+$  and  $\cdot\text{O}_2^-$  are the dominant active species during the degradation of TC. Besides, after recycling five times, the Ag0.1 sample maintained good adsorption and catalytic performance, suggesting that it has outstanding stability and recyclability. Based on the excellent performance of the  $\text{Ag}_2\text{S}/\text{TiO}_2$  composite fiber membrane in the photocatalytic and recycling process, the material has excellent prospects in the treatment of antibiotic wastewater pollution.

## Acknowledgements

This work was financially supported by the National Natural Science Foundation of China (51973100 and 51703102), China Geological Survey (Grant DD20189503), and the Natural Science Foundation of Shandong Province, China (No. ZR2019BF031).

## Author contributions

MD contributed to methodology, investigation, data curation, formal analysis, writing—original draft, and writing—review and editing. QHL contributed to investigation and formal analysis. RL contributed to validation, writing—review and editing. YQC contributed to writing—review and editing, funding acquisition, supervision, and project administration. XXW contributed to validation and software. JQY contributed to resources. YZL contributed to writing—review and editing, funding acquisition, and supervision.

## Compliance with ethical standards

**Conflict of interest** The authors declare that they have no known competing financial interests or personal relationships that could have appeared to influence the work reported in this paper.

**Electronic supplementary material:** The online version of this article (<https://doi.org/10.1007/s10853-021-05796-3>) contains supplementary material, which is available to authorized users.

## References

- [1] Ahmed MB, Zhou JL, Ngo HH, Guo W (2015) Adsorptive removal of antibiotics from water and wastewater: progress and challenges. *Sci Total Environ* 532:112–126. <https://doi.org/10.1016/j.scitotenv.2015.05.130>
- [2] Wang Y, Fu H, Yang X, An X, Zou Q, Xiong S, Han D (2020) Pt nanoparticles-modified  $\text{WO}_3/\text{TiO}_2$  core-shell ternary nanocomposites as stable and efficient photocatalysts in tetracycline degradation. *J Mater Sci* 55(29):14415–14430. <https://doi.org/10.1007/s10853-020-05014-6>

- [3] Yu H, Wang D, Zhao B, Lu Y, Wang X, Zhu S, Qin W, Huo M (2020) Enhanced photocatalytic degradation of tetracycline under visible light by using a ternary photocatalyst of  $\text{Ag}_3\text{PO}_4/\text{AgBr}/\text{g-C}_3\text{N}_4$  with dual Z-scheme heterojunction. *Sep Purif Technol* 237:116365–116374. <https://doi.org/10.1016/j.seppur.2019.116365>
- [4] Trovo AG, Nogueira RF, Aguera A, Fernandez-Alba AR, Malato S (2011) Degradation of the antibiotic amoxicillin by photo-Fenton process-chemical and toxicological assessment. *Water Res* 45(3):1394–1402. <https://doi.org/10.1016/j.watres.2010.10.029>
- [5] Gothwal R, Shashidhar T (2015) Antibiotic pollution in the environment: a review. *Clean: Soil, Air, Water* 43(4):479–489. <https://doi.org/10.1002/clen.201300989>
- [6] Zhang T, Liu Y, Rao Y, Li X, Zhao Q (2019) Enhanced photocatalytic activity of  $\text{TiO}_2$  with acetylene black and persulfate for degradation of tetracycline hydrochloride under visible light. *Chem Eng J* 384:123350. <https://doi.org/10.1016/j.cej.2019.123350>
- [7] Lei Y, Guo P, Jia M, Wang W, Liu J, Zhai J (2020) One-step photodeposition synthesis of  $\text{TiO}_2$  nanobelts/ $\text{MoS}_2$  quantum dots/rGO ternary composite with remarkably enhanced photocatalytic activity. *J Mater Sci* 55(30):14773–14786. <https://doi.org/10.1007/s10853-020-05067-7>
- [8] Choi SK, Kim S, Lim SK, Park H (2010) Photocatalytic comparison of  $\text{TiO}_2$  nanoparticles and electrospun  $\text{TiO}_2$  nanofibers: effects of mesoporosity and interparticle charge transfer. *J Physchemc* 114(39):16475–16480. <https://doi.org/10.1021/jp104317x>
- [9] Mali SS, Betty CA, Bhosale PN, Devan RS, Ma Y-R, Kolekar SS, Patil PS (2012) Hydrothermal synthesis of rutile  $\text{TiO}_2$  nanoflowers using Brønsted Acidic Ionic Liquid [BAIL]: synthesis, characterization and growth mechanism. *Cryst Eng Comm* 14(6):1920–1924. <https://doi.org/10.1039/c2ce06476f>
- [10] Xiao F (2012) Layer-by-Layer Self-assembly construction of highly ordered metal- $\text{TiO}_2$  nanotube arrays heterostructures (M/TNTs, M = Au, Ag, Pt) with tunable catalytic activities. *J Phys Chem C* 116(31):16487–16498. <https://doi.org/10.1021/jp3034984>
- [11] Asahi R, Morikawa T, Ohwaki T, Aoki K, Taga Y (2001) Visible-light photocatalysis in nitrogen-doped titanium oxides. *Science* 293(5528):269–271. <https://doi.org/10.1126/science.1061051>
- [12] Li Z, Fang Y, Zhan X, Xu S (2013) Facile preparation of squarylium dye sensitized  $\text{TiO}_2$  nanoparticles and their enhanced visible-light photocatalytic activity. *J Alloy Compd* 564:138–142. <https://doi.org/10.1016/j.jallcom.2013.03.002>
- [13] Zhang ZG, Liu H, Cui YQ, Dong M, Li QH, Wang XX, Ramakrishna S, Long YZ (2019) One step in situ loading of CuS nanoflowers on anatase  $\text{TiO}_2$ /polyvinylidene fluoride fibers and their enhanced photocatalytic and self-cleaning performance. *Nanoscale Res Lett* 14(1):215–228. <https://doi.org/10.1186/s11671-019-3052-5>
- [14] Khanchandani S, Srivastava PK, Kumar S, Ghosh S, Ganguli AK (2014) Band gap engineering of ZnO using core/shell morphology with environmentally benign  $\text{Ag}_2\text{S}$  sensitizer for efficient light harvesting and enhanced visible-light photocatalysis. *Inorg Chem* 53(17):8902–8912. <https://doi.org/10.1021/ic500518a>
- [15] Gholami M, Qorbani M, Moradlou O, Naseri N, Moshfegh AZ (2014) Optimal  $\text{Ag}_2\text{S}$  nanoparticle incorporated  $\text{TiO}_2$  nanotube array for visible water splitting. *RSC Adv* 4(15):7838–7844. <https://doi.org/10.1039/c3ra44898c>
- [16] Ong WL, Ho GW (2016) Enhanced photocatalytic performance of  $\text{TiO}_2$  hierarchical spheres decorated with  $\text{Ag}_2\text{S}$  Nanoparticles. *Proc Eng* 141:7–14. <https://doi.org/10.1016/j.proeng.2015.09.217>
- [17] Zuo Y, Chen J, Yang H, Zhang M, Wang Y, He G, Sun Z (2019) Ag- $\text{Ag}_2\text{S}$  quantum-dots modified  $\text{TiO}_2$  nanorod arrays with enhanced photoelectrochemical and photocatalytic properties. *J Alloy Compd* 780:347–354. <https://doi.org/10.1016/j.jallcom.2018.11.274>
- [18] Neves MC, Nogueira JMF, Trindade T, Mendonça MH, Pereira MI, Monteiro OC (2009) Photosensitization of  $\text{TiO}_2$  by  $\text{Ag}_2\text{S}$  and its catalytic activity on phenol photodegradation. *J Photochem Photobiol A* 204(2–3):168–173. <https://doi.org/10.1016/j.jphotochem.2009.03.014>
- [19] Chen Y, Kim H (2009) Preparation of superhydrophobic membranes by electrospinning of fluorinated silane functionalized poly (vinylidene fluoride). *Appl Surf Sci* 255(15):7073–7077. <https://doi.org/10.1016/j.apsusc.2009.03.043>
- [20] Ghafoor S, Ata S, Mahmood N, Arshad SN (2017) Photosensitization of  $\text{TiO}_2$  nanofibers by  $\text{Ag}_2\text{S}$  with the synergistic effect of excess surface  $\text{Ti}^{3+}$  states for enhanced photocatalytic activity under simulated sunlight. *Sci Rep* 7(1):255–265. <https://doi.org/10.1038/s41598-017-00366-7>
- [21] Yu D, Bai J, Liang H, Wang J, Li C (2015) A new fabrication of AgX (X = Br, I)- $\text{TiO}_2$  nanoparticles immobilized on polyacrylonitrile (PAN) nanofibers with high photocatalytic activity and renewable property. *RSC Adv* 5(111):91457–91465. <https://doi.org/10.1039/c5ra19235h>
- [22] Li Q-H, Dong M, Li R, Cui Y-Q, Xie G-X, Wang X-X, Long Y-Z (2021) Enhancement of Cr(VI) removal efficiency via adsorption/photocatalysis synergy using electrospun chitosan/ $\text{g-C}_3\text{N}_4/\text{TiO}_2$  nanofibers. *Carbohydr Polym*

- 253:117200–117211. <https://doi.org/10.1016/j.carbpol.2020.117200>
- [23] Liu F, Hashim NA, Liu Y, Abed MRM, Li K (2011) Progress in the production and modification of PVDF membranes. *J Membr Sci* 375(1–2):1–27. <https://doi.org/10.1016/j.memsci.2011.03.014>
- [24] Zhang ZG, Liu H, Wang XX, Zhang J, Yu M, Ramakrishna S, Long YZ (2019) One-step low temperature hydrothermal synthesis of flexible TiO<sub>2</sub>/PVDF@MoS<sub>2</sub> core-shell heterostructured fibers for visible-light-driven photocatalysis and self-cleaning. *Nanomaterials (Basel)* 9(3):431–453. <https://doi.org/10.3390/nano9030431>
- [25] Maria Angelin Sinthiya MKN, Ramamurthi K, Sethuraman K, Moorthy Babu S, Ramesh Babu R, Ganesh V (2018) Influence of heat treatment on the properties of hydrothermally grown 3D/1D TiO<sub>2</sub> hierarchical hybrid microarchitectures over TiO<sub>2</sub> seeded FTO substrates. *Appl Surf Sci* 449:122–131. <https://doi.org/10.1016/j.apsusc.2018.01.122>
- [26] de Mendonça VR, Lopes OF, Avansi W, Arenal R, Ribeiro C (2019) Insights into formation of anatase TiO<sub>2</sub> nanoparticles from peroxo titanium complex degradation under microwave-assisted hydrothermal treatment. *Ceram Int* 45(17):22998–23006. <https://doi.org/10.1016/j.ceramint.2019.07.345>
- [27] Bao S, Liang H, Li C, Bai J (2020) A heterostructure BiOCl nanosheets/TiO<sub>2</sub> hollow-tubes composite for visible light-driven efficient photodegradation antibiotic. *J Photochem Photobiol A* 397:112590–112600. <https://doi.org/10.1016/j.jphotochem.2020.112590>
- [28] Li H, Shan C, Pan B (2018) Fe(III)-doped g-C<sub>3</sub>N<sub>4</sub> mediated peroxymonosulfate activation for selective degradation of phenolic compounds via high-valent iron-oxo species. *Environ Sci Technol* 52(4):2197–2205. <https://doi.org/10.1021/acs.est.7b05563>
- [29] Huo P, Liu C, Wu D, Guan J, Li J, Wang H, Tang Q, Li X, Yan Y, Yuan S (2018) Fabricated Ag/Ag<sub>2</sub>S/reduced graphene oxide composite photocatalysts for enhancing visible light photocatalytic and antibacterial activity. *J Ind Eng Chem* 57:125–133. <https://doi.org/10.1016/j.jiec.2017.08.015>
- [30] Yadav SK, Jeevanandam P (2015) Synthesis of Ag<sub>2</sub>S-TiO<sub>2</sub> nanocomposites and their catalytic activity towards rhodamine B photodegradation. *J Alloy Compd* 649:483–490. <https://doi.org/10.1016/j.jallcom.2015.07.184>
- [31] Ren H, Xu W, Zhu S, Cui Z, Yang X, Inoue A (2016) Synthesis and properties of nanoporous Ag<sub>2</sub>S/CuS catalyst for hydrogen evolution reaction. *Electrochim Acta* 190:221–228. <https://doi.org/10.1016/j.electacta.2015.12.096>
- [32] Ho W, Yu JC, Lee S (2006) Synthesis of hierarchical nanoporous F-doped TiO<sub>2</sub> spheres with visible light photocatalytic activity. *Chem Commun* 10:1115–1117. <https://doi.org/10.1039/b515513d>
- [33] Neelgund GM, Oki A (2011) Photocatalytic activity of CdS and Ag<sub>2</sub>S quantum dots deposited on poly (amidoamine) functionalized carbon nanotubes. *Appl Catal B* 110:99–107. <https://doi.org/10.1016/j.apcatb.2011.08.031>
- [34] Liqiang J, Honggang F, Baiqi W, Dejun W, Baifu X, Shudan L, Jiazhong S (2006) Effects of Sn dopant on the photoinduced charge property and photocatalytic activity of TiO<sub>2</sub> nanoparticles. *Appl Catal B* 62(3–4):282–291. <https://doi.org/10.1016/j.apcatb.2005.08.012>
- [35] Yang Y, Wen J, Wei J, Xiong R, Pan CX (2013) Polypyrrole-decorated Ag-TiO<sub>2</sub> nanofibers exhibiting enhanced photocatalytic activity under visible-light illumination. *ACS Appl Mater Interfaces* 5(13):6201–6207. <https://doi.org/10.1021/am401167y>
- [36] Khan SUM, Akikusa J (1999) Photoelectrochemical splitting of water at nanocrystalline n-Fe<sub>2</sub>O<sub>3</sub> thin-film electrodes. *J Phys Chem B* 103:7184–7189. <https://doi.org/10.1021/jp990066k>
- [37] Huang L, Fang W, Yang Y, Wu J, Yu H, Dong X, Wang T, Liu Z, Zhao B (2018) Three-dimensional MoO<sub>3</sub> nanoflowers assembled with nanosheets for rhodamine B degradation under visible light. *Mater Res Bull* 108:38–45. <https://doi.org/10.1016/j.materresbull.2018.08.036>
- [38] Zhu Y, Xu D, Meng M (2015) Ultrasonic-assisted synthesis of amorphous Bi<sub>2</sub>S<sub>3</sub> coupled (BiO)<sub>2</sub>CO<sub>3</sub> catalyst with improved visible light-responsive photocatalytic activity. *J Mater Sci* 50(4):1594–1604. <https://doi.org/10.1007/s10853-014-8720-3>
- [39] Liu N, Guo Y, Yang X, Lin H, Yang L, Shi Z, Zhong Z, Wang S, Tang Y, Gao Q (2015) Microwave-assisted reactant-protecting strategy toward efficient MoS<sub>2</sub> electrocatalysts in hydrogen evolution reaction. *ACS Appl Mater Interfaces* 7(42):23741–23749. <https://doi.org/10.1021/acsami.5b08103>
- [40] Wei Z, Xinyue T, Xiaomeng W, Benlin D, Lili Z, Jiming X, Yue F, Ni S, Fengxia Z (2019) Novel p-n heterojunction photocatalyst fabricated by flower-like BiVO<sub>4</sub> and Ag<sub>2</sub>S nanoparticles: simple synthesis and excellent photocatalytic performance. *Chem Eng J* 361:1173–1181. <https://doi.org/10.1016/j.cej.2018.12.120>
- [41] Gao Y, Li Y, Zhang L, Huang H, Hu J, Shah SM, Su X (2012) Adsorption and removal of tetracycline antibiotics from aqueous solution by graphene oxide. *J Colloid Interface Sci* 368(1):540–546. <https://doi.org/10.1016/j.jcis.2011.11.015>
- [42] Zhang S, Yang Y, Xu L, Yu H, Li D, Wang X, Dong X (2020) A facile one-step synthesis of super-hydrophilic (NH<sub>4</sub>)<sub>0.33</sub>WO<sub>3</sub>/WS<sub>2</sub> composites: a highly efficient adsorbent

- for methylene blue. *New J Chem* 44:10418–10427. <https://doi.org/10.1039/D0NJ01075H>
- [43] Herrmann J-M, Tahari H, Ait-Ichou Y, Lassaletta G, Gonzalez-Elipe AR, Fernbdez A (1997) Characterization and photocatalytic activity in aqueous medium of TiO<sub>2</sub> and Ag-TiO<sub>2</sub> coatings on quartz. *Appl Catal B Environ* 13(3–4):219–228. [https://doi.org/10.1016/s0926-3373\(96\)0107-5](https://doi.org/10.1016/s0926-3373(96)0107-5)
- [44] Liu H, Zhang Z-G, Wang X-X, Nie G-D, Zhang J, Zhang S-X, Cao N, Yan S-Y, Long Y-Z (2018) Highly flexible Fe<sub>2</sub>O<sub>3</sub>/TiO<sub>2</sub> composite nanofibers for photocatalysis and ultraviolet detection. *J Phys Chem Solids* 121:236–246. <https://doi.org/10.1016/j.jpcs.2018.05.019>
- [45] Yan M, Wu Y, Liu X (2021) Photocatalytic nanocomposite membranes for high-efficiency degradation of tetracycline under visible light: An imitated core-shell Au-TiO<sub>2</sub>-based design. *J Alloy Compd* 855:157548–157557. <https://doi.org/10.1016/j.jallcom.2020.157548>
- [46] Ma D, Liu W, Chen Q, Jin Z, Zhang Y, Huang J, Zhang H, Peng F, Luo T (2021) Titanium-oxo-clusters precursors for preparation of In<sub>2</sub>S<sub>3</sub>/TiO<sub>2</sub> heterostructure and its photocatalytic degradation of tetracycline in water. *J Solid State Chem* 293:121791–121801. <https://doi.org/10.1016/j.jssc.2020.121791>
- [47] Shi Y, Yang Z, Wang B, An H, Chen Z, Cui H (2016) Adsorption and photocatalytic degradation of tetracycline hydrochloride using a palygorskite-supported Cu<sub>2</sub>O-TiO<sub>2</sub> composite. *Appl Clay Sci* 119:311–320. <https://doi.org/10.1016/j.clay.2015.10.033>
- [48] Hu X, Zhang G, Yin C, Li C, Zheng S (2019) Facile fabrication of heterogeneous TiO<sub>2</sub>/BiOCl composite with superior visible-light-driven performance towards Cr(VI) and tetracycline. *Mater Res Bull* 119:110559–110568. <https://doi.org/10.1016/j.materresbull.2019.110559>
- [49] Wang H, Wu X, Zhao H, Quan X (2012) Enhanced photocatalytic degradation of tetracycline hydrochloride by molecular imprinted film modified TiO<sub>2</sub> nanotubes. *Chin Sci Bull* 57(6):601–605. <https://doi.org/10.1007/s11434-011-4897-x>
- [50] Wang P, Yap P-S, Lim T-T (2011) C-N-S tridoped TiO<sub>2</sub> for photocatalytic degradation of tetracycline under visible-light irradiation. *Appl Catal A* 399(1–2):252–261. <https://doi.org/10.1016/j.apcata.2011.04.008>
- [51] Deng Y, Tang L, Zeng G, Wang J, Zhou Y, Wang J, Tang J, Wang L, Feng C (2017) Facile fabrication of mediator-free Z-scheme photocatalyst of phosphorous-doped ultrathin graphitic carbon nitride nanosheets and bismuth vanadate composites with enhanced tetracycline degradation under visible light. *J Coll Interface Sci* 509:219–234. <https://doi.org/10.1016/j.jcis.2017.09.016>
- [52] Zhao L, Luo X, Luo S, Dionysiou DD (2018) Highly efficient visible-light photocatalytic performance of Ag/AgIn<sub>5</sub>S<sub>8</sub> for degradation of tetracycline hydrochloride and treatment of real pharmaceutical industry wastewater. *Chem Eng J* 333:423–433. <https://doi.org/10.1016/j.cej.2017.09.022>
- [53] Zeng Y, Guo N, Li H-Y, Wang Q-Y, Xu X-J, Y Y, Han Xue-R, (2018) Construction of flower-like MoS<sub>2</sub>/Ag<sub>2</sub>S/Ag Z-scheme photocatalysts with enhanced visible-light photocatalytic activity for water purification. *Sci Total Environ* 659:20–32. <https://doi.org/10.1016/j.scitotenv.2018.12.333>
- [54] Chen X, Zhang W, Zhang L, Feng L, Wen J, Yang J, Zhang C, Jiang J, Wang H (2019) Effective photocatalytic salicylic acid removal under visible light irradiation using Ag<sub>2</sub>S/AgI-Bi<sub>2</sub>S<sub>3</sub>/BiOI with Z-scheme heterojunctions. *Appl Surf Sci* 481:1335–1343. <https://doi.org/10.1016/j.apsusc.2019.03.214>
- [55] Minmin Gaoa LZ, Peha CKN, Ho GW (2017) Functionalization of TiO<sub>2</sub> nanofibers with Ag and Ag<sub>2</sub>S nanoparticles for enhanced photocatalytic hydrogen generation. *Proc Eng* 215:188–194. <https://doi.org/10.1016/j.proeng.2017.11.008>
- [56] Hu X, Li Y, Tian J, Yang H, Cui H (2017) Highly efficient full solar spectrum (UV-vis-NIR) photocatalytic performance of Ag<sub>2</sub>S quantum dot/TiO<sub>2</sub> nanobelt heterostructures. *J Ind Eng Chem* 45:189–196. <https://doi.org/10.1016/j.jiec.2016.09.022>

**Publisher's Note** Springer Nature remains neutral with regard to jurisdictional claims in published maps and institutional affiliations.